Modeling the kinetic behavior of the Li-RHC system for energy-hydrogen storage: (I) absorption

A.M. Neves [a,b,*], J. Puszkiel [b,c], G. Capurso [b], J.M. Bellosta von Colbe [b], C. Milanese [d], M. Dornheim [b], T. Klassen [a,b], J. Jepsen [a,b]

[a] Helmut Schmidt University (HSU), University of the Federal Armed Forces, Holstenhofweg 85, 22043, Hamburg, Germany
[b] Helmholtz-Zentrum Hereon, Institute of Hydrogen Technology, Max-Plank-Str. 1, 21502, Geesthacht, Germany
[c] IREC Catalonia Institute for Energy Research, 08930, Sant Adrià de Besòs, Barcelona, Spain
[d] Pavia H2 Lab, C.S.G.I. & Department of Chemistry, Physical Chemistry Section, University of Pavia, 27100, Pavia, Italy

HIGHLIGHTS

- Experimental determination of hydrogenation thermodynamic parameters.
- Critical analysis of the reported hydrogenation thermodynamic data.
- Development of a comprehensive semi-empirical absorption kinetic model.
- One-dimensional interface-controlled reaction upon hydrogenation.

GRAPHICAL ABSTRACT
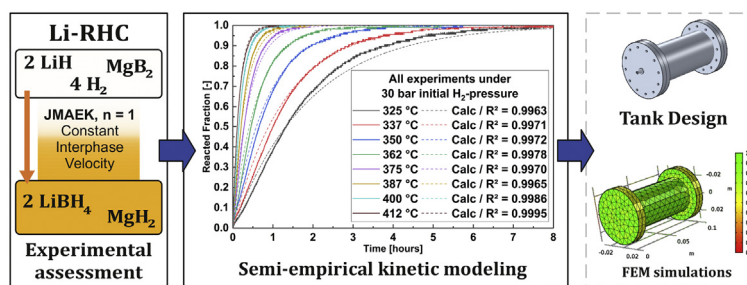
ARTICLE INFO

ABSTRACT

The Lithium–Boron Reactive Hydride Composite System (Li-RHC) (2 LiH + MgB$_2$/2 LiBH$_4$ + MgH$_2$) is a high-temperature hydrogen storage material suitable for energy storage applications. Herein, a comprehensive gas-solid kinetic model for hydrogenation is developed. Based on thermodynamic measurements under absorption conditions, the system's enthalpy ΔH and entropy ΔS are determined to amount to $-34 \pm 2\,\mathrm{kJ \cdot mol\,H_2^{-1}}$ and $-70 \pm 3\,\mathrm{J \cdot K^{-1} \cdot mol\,H_2^{-1}}$, respectively. Based on the thermodynamic behavior assessment, the kinetic measurements' conditions are set in the range between 325 °C and 412 °C, as well as between 15 bar and 50 bar. The kinetic analysis shows that the hydrogenation rate-limiting-step is related to a one-dimensional interface-controlled reaction with a driving-force-corrected apparent activation energy of $146 \pm 3\,\mathrm{kJ \cdot mol\,H_2^{-1}}$. Applying the kinetic model, the dependence of the reaction rate constant as a function of pressure and temperature is calculated, allowing the design of optimized hydrogen/energy storage vessels *via* finite element method (FEM) simulations.

© 2021 Hydrogen Energy Publications LLC. Published by Elsevier Ltd. All rights reserved.

Introduction

Mainly driven by the necessity of reducing the impact of fossil energy consumption on the environment, researchers have been looking for suitable alternatives for generation, storage and use of renewable energies. One of the most promising alternatives is the use of hydrogen as an energy carrier, which can significantly reduce the negative impact on the environment if the hydrogen is produced from renewable sources [1,2].

Current technology can produce hydrogen by several methods is able to produce [3] and convert it for utilization [4]. Not only hydrogen production but also its conversion and its storage are topics under intense investigation. Nowadays, a cost-effective, compact and safe system to store hydrogen represents a bottleneck for the broad implementation of hydrogen as a clean energy vector.

Today, physical storage methods are the most widely used technologies. While readily available, pressurized vessels and liquefied hydrogen have disadvantages involving inherent safety risks and the necessity of operating in extreme conditions (e.g., pressures up to 700 bar for gaseous or temperatures below the critical temperature −240.15 °C − or even below −252,15 °C considering ambient pressure − for liquid hydrogen), increasing the overall operation costs of such technologies [5]. A considerable amount of the energy stored in hydrogen is required for its liquefaction [6,7] or its compression to increase the stored hydrogen density [6]. Chemical storage methods, such as hydrides, are an alternative to the physical methods mentioned above and show technological potential since they can work under much milder conditions of pressure and temperature [5].

One of the main challenges to store hydrogen efficiently is related to the low volumetric energy density that can be achieved by the current hydrogen storage technologies; especially if mobile applications are envisioned. For hydrogen gas, the volumetric energy density is around 3 kWh·m^{-3} under STP conditions [8—10]. Even though this value can be improved by using the aforementioned physical storage methods, the use of hydrides offers the advantage of reaching a value of up to 150 kg H$_2$·m^{-3} with the Mg$_2$FeH$_6$ complex hydride (equivalent to around 5000 kWh·m^{-3} [11]). By working under milder conditions, hydrides allow avoiding energy losses in compression in the case of gas-high pressure storage and boil-off in the case of cryogenic storage [12].

One of the highest hydrogen volumetric and gravimetric densities is found in the light-complex hydride LiBH$_4$, presenting a volumetric storage density of a theoretical value of 121 kg H$_2$·m^{-3} [13,14]. LiBH$_4$ decomposes only at temperatures over 400 °C, releasing H$_2$, LiH and B as products. LiBH$_4$ has a theoretical hydrogen gravimetric capacity of 13.5 wt %, considering its decomposition to LiH, B and H$_2$. This is because LiH is stable up to 900 °C [15]. Additionally, pristine LiBH$_4$ has rather poor reversibility, even under harsh conditions (over 400 °C and 100 bar) [16].

In order to overcome these limitations, several approaches have been applied such as nanoconfinement, addition of transition metals, destabilization through different complexes and binary hydrides addition [17—21]. Among them, the so-called Reactive Hydride Composite (RHC) approach has been one of the most effective methods with potential for a practical application owing to its suitable hydrogen storage properties [9,17]. The use of boron compounds (MgB$_2$) instead of elemental boron to synthesize light borohydrides like LiBH$_4$, NaBH$_4$ and Ca(BH$_4$)$_2$ (among others) by gas-phase loading has been studied by Barkhordarian et al. [17]. By the combining 1 mol MgH$_2$ with 2 mol LiBH$_4$ a fully-reversible composite system could be obtained [22]. In this material (hereafter named Li-RHC), the theoretical absorption reaction under around 400 °C proceeds as follows [22,23]:

$$2\,LiH + MgB_2 + 4\,H_2 \rightarrow 2\,LiBH_4 + MgH_2 \tag{1}$$
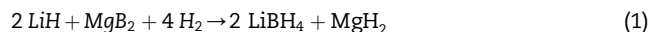
Under this assumption, the reaction proceeds in a one-step fashion, with the reactants' consumption considered to occur concomitantly. The overall absorption reaction is exothermal. It is however important to see that the decomposition of the stable MgB$_2$ (standard enthalpy of formation of MgB$_2$ is ΔH = −92.0 kJ·mol^{-1}) is endothermal [24]. Therefore, the overall enthalpy of reaction decreases, allowing the formation of LiBH$_4$, otherwise difficult to obtain. Thermodynamic calculations have shown that the theoretical reaction enthalpy of Eq. (1) amounts to −46 kJ·mol H$_2^{-1}$ [17]. Absorption and desorption behaviors are, however, markedly different for this material [25], what brings even more challenges for interpreting data and greatly limits the applicability of conclusions drawn from experimental investigations and theoretical calculations to their respective case-scenarios.

This reaction is generally accepted [22,23,25—32] as representative of the absorption process and proceeds as a one-step reaction [25,28]. However, it was first suggested by Vajo et al. [22] that between 400 and 450 °C a two-plateau region should exist. Cova et al. [23] have shown that after around 413 °C a two-plateau region can be seen. These plateaus are related to the equilibrium conditions of the LiBH$_4$ phase and the Mg/MgH$_2$ reaction. Although such expected transition has been observed in previous works, enthalpy and entropy values are seemingly in disagreement even for the single-plateau temperature range among different works [22,23,33]. The kinetic properties of the system are influenced fundamentally by temperature and pressure. However, they are also affected by many other factors, including, for example, the reacted fraction, use of additives (catalysts) [22,25—32,34], microstructure, particle size distribution [35], cycle number [9], and degree of compaction [36], among others.

Envisioning the application of Li-RHC in a hydrogen storage system, a complete kinetic and thermodynamic investigation is required. With this information, it is possible to develop kinetic models that describe the reaction rate of the material as a function of the reacted fraction, the operative pressure and the temperature. One of the main challenges in the design of hydrogen storage systems based on hydrides lays on the development of numerical models that describe the phenomena occurring upon hydrogenation and dehydrogenation. Trustable models allow to evaluate the practical feasibility of the system, reducing the time and costs associated with experimental evaluations. Furthermore, the numerical development can lead to the identification of the most relevant

parameters, so that the design can be optimized, either by purely numerical methods or by its combination with novel computational approaches such as machine learning [37].

This work aims to develop a comprehensive kinetic model for the absorption reaction of Li-RHC (2 MgH_2 + $LiBH_4$) with 0.05 mol $TiCl_3$ as an additive. For this purpose, the assessment of the thermodynamic behavior is performed, as well as investigations of its kinetic properties. These results enabled the determination of the rate-limiting step of the hydrogenation process, the identification of the driving-force component and consequently, the calculation of apparent activation energy for the absorption reaction under a wide range of pressure and temperature conditions. Finally, the calculations allow the identification of a general equation that describes the kinetic behavior of the system for the chosen experimental conditions. To the best of our knowledge, this is the first time that a comprehensive kinetic model for the hydrogenation of Li-RHC is presented, which contributes with new insights for forthcoming investigations about the modeling and design of hydrogen-energy storage reservoirs.

Experimental

Material preparation

High-energy ball-milling (HEBM)

For the preparation of the Li-RHC, LiH powder (Alfa Aesar, purity of ≥99.4%) and MgB_2 powder (Alfa Aesar, purity of 99%) were mixed in a 2:1 M ratio. Then, 0.05 mol of $TiCl_3$ (Sigma Aldrich, purity ≥ 99.995%) per mol of MgB_2 was added. The milling process was carried out in a planetary ball-milling device (Fritsch, Pulverisette 5, Germany) using a 76 mm diameter tempered steel milling vial (66 mm high) with 10 mm tempered steel balls under argon atmosphere, a BPR (ball mass to powder mass ratio) of 10:1, for a total milling time of 20 h (4 h milling, followed by 1 h wait time, repeated 4 times), at 230 RPM, with 20% of volume filling (ball volume with respect to the vial internal volume). For each milling, an amount of 5 g of powder was inserted into the milling vial. These parameters were chosen based on analyses developed and thoroughly discussed in previous work [35]. The as-milled powder present the following characteristics: particle size ranging from 10 to 70 μm, surface area of about 15 m^2/g and a rounded-platelet-like morphology [35].

All the handling was performed under argon atmosphere and the storage of the samples was done in a continuously purified argon-filled glove box (MBraun, Germany).

Kinetics and thermodynamical properties assessment

Intrinsic kinetic measurements, data handling and PCI curves
The hydrogen absorption experiments to assess intrinsic kinetic[*] behaviors were performed using a Sieverts-type

---

[*] "Intrinsic Kinetic" is here understood as the kinetics of hydrogen absorption reaction taken as a whole (with its many steps) that is, for every practical purpose, devoid of influence of heat management and mass flow limitations for the optimal proceeding of the reaction.

apparatus (HERA, Canada, Canadian Patent, Serial Number 2207149 [38]) equipped with a differential pressure sensor and calibrated volumes. The internal apparatus temperature was maintained at 40 ± 1 °C at all times. The sample heating was provided by an oven surrounding the whole sample holder. The thermocouple used to assess the temperature during the experiment was located on the sample holder's outer wall.

For these measurements, around 100–150 mg of material were used to assure isothermal and isobaric conditions, as well as homogeneous concentration changes in the mass of material. With this, the mass of material can be considered as a punctual mass, avoiding the influence of heat transfer and mass transport phenomena [39]. This condition is also taken in several works [9,25,27,34,48] applying gas-solid models to fit the experimental curves, in which the used mass ranges between 100 and 200 mg. The use of more mass can cause a deviation in the analysis of the intrinsic kinetic model, and mainly create a non-uniform temperature profile in the sample, so that one have neither isothermal nor homogeneous concentration changes in the used mass of material. Such condition leads to mismatch in the real intrinsic kinetic behavior, since the equilibrium pressure of the material in different parts would be different as the temperature changes, leading to a concentration profile in the material [39].

The experiments were performed starting at the 18th cycle to ensure that the material was already stabilized in terms of capacity and kinetic behavior (see also Fig. S1 and Fig. S2 of the Supplementary Material). The two sets of experiments were kinetic measurements at constant pressure (30 bar), with varying temperatures ranging from 312 °C up to 425 °C (10 measurements in regular intervals), and kinetic measurements at constant temperature (375 °C) with varying pressures, from 15 bar to 50 bar (with a step of 5 bar).

The acquired data was batch-processed with a specific Python (Python 3.7) script and further treated in OriginPro™ version 9.6.0.172 Software (Origin Lab Corporation). The fittings and statistical evaluation employed user-defined functions, which were added with the in-built tools of the program. The expression used for uncertainty propagation is shown in Eq. (S1) in the Supplementary Material.

The Pressure-Composition-Isotherms curves were acquired between 350 °C and 425 °C using a PCT Pro (SETARAM, Caluire, France) at the University of Pavia, Italy. A mass of approximately 150 mg was used. The amount of absorbed hydrogen was normalized as reacted fraction according to Eq. (2) for each of the curves individually.

$$\alpha = \frac{mH_{2,\,t}}{mH_{2,\,max}} \qquad (2)$$

where $mH_{2,\,t}$ is the mass of hydrogen absorbed at a given time t after the experiment started, $mH_{2,\,max}$ is the maximum capacity reached at the time in which the experiment was terminated. Reacted fraction values are experimentally determined and always vary from 0 to 1.

To determine ΔH and ΔS via van't Hoff equation, the hydrogenation process of the studied material was considered as a single-step process. The start and end of the plateau region where taken, respectively, as 0.2 and 0.7. For these calculations, the mean value of the temperature T_{mean} throughout the experiment was considered.

The ΔH and ΔS are explicitly considered with a negative sign, since the hydrogen absorption reaction is exothermic.

Kinetic modeling

Empirical kinetic model and general definitions

The approach used in the present work is the Separable Variable approach as described by Eq. (3) [40,41]. In this model, it is possible to obtain the variation of the reacted fraction α as a function of time t by determining three variables, namely, K(T), F(P) and G(α). The name of this method of deriving a kinetic model comes from its strategy, which implies: by keeping two (undetermined) variables constant, it is possible to determine the third one. By reorganizing the variables and keeping some of those constant, all of the variables can be determined.

$$\frac{d\alpha}{dt} = K(T) \cdot F(P) \cdot G(\alpha) \tag{3}$$

The G(α) term in Eq. (3) corresponds to the dependency of the reaction rate on intrinsic factors (defects, crystalline structure, etc.) and morphological changes of the particles (size and geometry) [42,43]. G(α) is represented by different expressions according to the gas-solid reaction model and as a function of the quantity reacted fraction α [40].

These different gas-solid kinetic models belong to different categories and each implies a rate-limiting step for the overall reaction progress. In Table 1, it is possible to see a description of the gas-solid models with their names, differential form G(α), integral form g(α), acronym taken in this work and corresponding references. There is a large number of gas-solid models, and thus only some of the best-fitting models considered in the present work as possible candidates are shown. For the complete table, please refer to Supplementary Material Table S1. For a more in-depth discussion of the application of these gas-solid kinetic models, please refer to the work of Puszkiel [40].

The kinetic constant can be expressed as a function of the temperature and pressure functionalities, as described in Eq. (4):

$$k(T, P) = K(T) \cdot F(P) \tag{4}$$

K(T) represents the temperature-dependent term. This functionality is defined by the Arrhenius form, as shown in Eq. (5).

$$K(T) = A \cdot \exp\left(\frac{-E_a}{R \cdot T}\right) \tag{5}$$

where A is the frequency factor (also called pre-exponential factor) and E_a is the apparent activation energy (of the reaction occurring in the material as a whole).

The pressure-dependency component F(P) is related to the chemical reaction's driving force. This component includes the operative pressure P and the equilibrium pressure P_{eq}. The precise form of F(P) is not easily determined and it is usually tentatively chosen among possible candidates, which are functions of parameters mentioned above. For the sake of clarity, Table 3 in Section Determination of temperature K(T) and pressure F(P) functionalities shows the tentatively used expressions in the attempt of fitting the experimental data.

To calculate the F(P) values, the P_{eq} expression was obtained from the entropy ΔH and enthalpy ΔS values by using the van't Hoff equation as described by Eq. (6) in Section Thermodynamical properties. In all the calculations, the temperature and pressure were taken as the mean temperature T_{mean} and mean pressure P_{mean} throughout the course of the experiment.

A simplified description of the steps to perform such calculations is provided below.

1. A set of curves under the same H_2-pressure under different (but quasi-constant) T are collected. For each of these curves, K(T) and F(P) are assumed constant. By calculating the reacted fraction α from the experimentally acquired kinetic curves from 10 to 90% of α it is possible to evaluate which reaction model G(α) best represents the kinetics of the studied system. The "reduced time method" proposed by Sharp et al. [49] and Jones et al. [50] was used for this determination. For additional information, please refer to the Supplementary Material;
2. Once a reaction model was assumed, a non-linear fit considering the integrated form g(α) is used to obtain individual sets of k (T, P) from the experimental data;
3. With these values of k (T, P), a first determination of the frequency factor A and the apparent activation energy E_a is done by considering a reaction model G(α) and F(P) as constant for each curve. The values found here are not the final ones and new values are assumed in the following steps;

Table 1 – Four of the best-fitting kinetic models.

Model	Rate-Limiting Step	Differential form G(α)	Integrated Form g(α) = k*t	Acronym	Ref.
Johnson-Mehl-Avrami-Erofeyev-Kholmogorov, n = 1	One-dimensional growth with interface-controlled reaction rate	$(1 - \alpha)$	$-\ln(1 - \alpha)$	JMAEK, n = 1	[9,25,40, 41,44–48]
Johnson-Mehl-Avrami-Erofeyev-Kholmogorov, n = 1.5	Three-dimensional growth of random nuclei with decreasing diffusion-controlled reaction rate	$\frac{3}{2}(1 - \alpha)[(-\ln(1 - \alpha)]^{\frac{1}{3}}$	$[-\ln(1 - \alpha)]^{\frac{2}{3}}$	JMAEK, n = 1.5	[34,40,47]
Contracting Area	Two-dimensional growth of contracting cylindrical volume	$2(1 - \alpha)^{\frac{1}{2}}$	$1 - (1 - \alpha)^{\frac{1}{2}}$	CA	[40,41,47]
Contracting Volume	Three-dimensional growth of contracting sphere	$2(1 - \alpha)^{\frac{1}{3}}$	$1 - (1 - \alpha)^{\frac{1}{3}}$	CV	[25,27,34, 40,41,47]

4. Assuming the calculated A, E_a, and the reaction model $G(\alpha)$, the different pressure-dependency term F(P) expressions are evaluated. After evaluation, if a suitable expression is found, new values for the frequency factor A and the apparent activation energy E_a are assumed, thus, this is an iterative process;

5. With the determination of K(T), F(P) and $G(\alpha)$, it is now possible to perform the data validation by plotting the calculated and the experimental reacted fraction α against time t curves.

For the determination of a general reaction model expression, some remarks should be taken into consideration. First, the models presented here were originally developed for the modeling of nucleation and growth kinetics considering liquid-solid (solidification) and solid-solid interactions [44−46]. Later, these same models were adapted for gas-solid interactions for hydride kinetic modeling. In the present case, all the kinetic measurement temperatures are above 270 °C, which is the melting point for the $LiBH_4$ phase [28]. However, the fact that one of the phases is in the liquid state was not considered in this analysis. This is possible particularly because these models presuppose themselves the existence of a rate-limiting step for the reaction. The gas-solid model describes the changes of the materials upon hydrogenation and dehydrogenation based on the fitting of such models to experimental curves. An analysis of this complex system at the atomic level is out of the scope of this work. Moreover, the overall reaction, as shown in Eq. (1), considers that the reaction occurs as a single-step reaction. All these simplifications were taken and validated in previous works about the analysis of the rate-limiting step of this complex hydride system [9,25,48].

Table 2 − Fitting parameters for the three highest-ranking models for four chosen temperatures, under 30 bar of initial hydrogen pressure.

Model	Fit Parameter	312 °C	350 °C	400 °C	412 °C
JMAEK, n = 1	R^2	0.996	0.999	0.999	0.999
	Slope	1.421 ± 0.002	1.183 ± 0.001	1.208 ± 0.001	0.968 ± 0.002
	Y-Intercept	−0.369 ± 0.003	−0.145 ± 0.002	−0.073 ± 0.001	0.051 ± 0.004
JMAEK, n = 1.5	R^2	0.995	0.992	0.991	0.986
	Slope	0.841 ± 0.001	0.696 ± 0.002	0.717 ± 0.001	0.564 ± 0.005
	Y-Intercept	0.137 ± 0.002	0.277 ± 0.003	0.321 ± 0.002	0.401 ± 0.010
Contracting Volume (CV)	R^2	0.995	0.993	0.991	0.987
	Slope	1.091 ± 0.002	0.903 ± 0.002	0.932 ± 0.001	0.735 ± 0.006
	Y-Intercept	−0.097 ± 0.003	0.084 ± 0.004	0.139 ± 0.003	0.245 ± 0.012

Table 3 − Summary of the F(P) expressions with conditions for utilization and/or conditions: mathematical expression, name used in this work and corresponding reference(s).

Limited	Category/Conditions	Expression	Name	Reference
$F(P) > 0$	$P = P_{eq} \Rightarrow F(P) \neq 0$	$\dfrac{P}{P_{eq}}$	F1	[52]
	$P = P_{eq} \Rightarrow F(P) = 0$	$P - P_{eq}$	F2	[53−56]
		$\dfrac{P - P_{eq}}{P_{eq}}$	F3	[57]
		$P^{0.5} - P_{eq}^{0.5}$	F4	[55,58]
		$\left(\dfrac{P_{eq} - P}{P_{eq}}\right)^2$	F5	[59]
		$\ln\left(\dfrac{P}{P_{eq}}\right)$	F6	[56,60−63]
	$F(P)$ not a function of P_{eq}	P	F7	[64]
	$F(P)$ not a function of P_{eq} $\quad P_{eq} \approx 0$	$P^{0.5}$	F8	[65]
$0 \leq F(P) < 1$	$P = P_{eq} \Rightarrow F(P) = 0$	$1 - \left(\dfrac{P_{eq}}{P}\right)^{0.5}$	F9	[59,66,67]
	$P = P_{eq} \Rightarrow F(P) = 0$ $\quad P_{eq} < P \leq 2P_{eq}$	$\dfrac{\lvert P_{eq} - P \rvert}{P_{eq}}$	-[a]	[68]

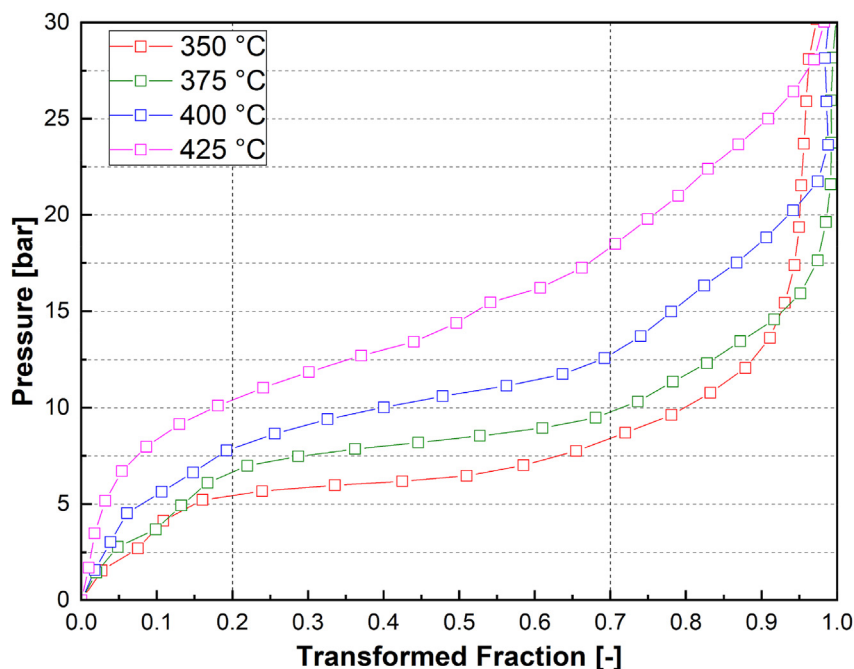[a] This expression is numerically identical to F3 expression.

Fig. 1 – Pressure-composition-isotherm (PCI) curves for the studied Li-RHC at different temperatures under absorption conditions. The vertical lines indicate the points that were used for the thermodynamic parameter calculation.

Results and discussion

Thermodynamical properties

Fig. 1 shows the hydrogenation pressure-composition isotherms measured in the range between 350 °C and 425 °C. The PCIs display a notable variation of the equilibrium pressure P_{eq} with the amount of absorbed hydrogen (transformed fraction), which gives rise to a "sloped" plateau.

The thermodynamic parameters enthalpy ΔH and entropy ΔS can be calculated from the measured equilibrium pressure P_{eq} by applying the van't Hoff Eq. (6). At each temperature, the P_{eq} was determined as a mean value between 0.2 and 0.7 of the transformed fraction α. Furthermore, a mean temperature T_{mean} was taken considering the whole duration of the experiment. The P_0 is the thermodynamic reference pressure (considered 1 bar).

$$\ln\left(\frac{P_{eq}}{P_0}\right) = \left(\frac{\Delta H}{R \cdot T}\right) - \left(\frac{\Delta S}{R}\right) \qquad (6)$$

By determining enthalpy ΔH and entropy ΔS values, it is possible to calculate an equilibrium pressure P_{eq} as a function of the temperature T.

A comparative evaluation of the results for ΔH and ΔS and the pressure ranges reported in the literature is seen in Fig. 2. The data points in Fig. 2 were taken from the works of Vajo et al. [22], Cova et al. [23], Puszkiel [33] and this work. The values shown in the diagram are recalculated values as per reported in these works. Since only one of the works, namely,

the one from Vajo et al., reported the value for ΔS, for consistency, the recalculated values are instead being shown. Still, the differences between the recalculated values and the reported values were significantly different only for the single plateau for the work of Cova et al. [23]. A complete table with the used pressure values, the fitting parameters, the calculated and reported values is available in Table S2 in the Supplementary Material.

The straight lines represent the linear regression performed with the points shown in the diagram. The dashed line at around 412 °C is an approximation for the temperature range after which the reaction would not occur as a one-step reaction.

Vajo et al. [22] has reported that the ΔH and ΔS for this system amounts to $-40.5 \text{ kJ} \cdot \text{mol H}_2^{-1}$ and $-81.3 \text{ J} \cdot \text{K}^{-1} \cdot \text{mol H}_2^{-1}$. Moreover, it has been proposed that the rise of a two-plateau reaction could possibly be observed for higher temperatures [22]. The data provided for the 450 °C PCI on that work could not resolve this issue. Later on, works from Puszkiel [33] and Cova et al. [23] have both been able to measure the presence of two plateaus for temperatures over 400 °C–412 °C, respectively. In this range of temperatures, the system presents a region between the lower ($LiBH_4$) and upper plateau (Mg/MgH_2) in which it is theoretically possible to have coexistence of $LiBH_4$ and Mg in equilibrium conditions. This two-plateau behavior, however, is not clearly visible in the results presented in this work. This fact can be attributed to the differences in the equilibrium conditions resulting from differences in starting materials, handling, processing, among other experimental conditions. It should be expected that such a two-region plateau exists even
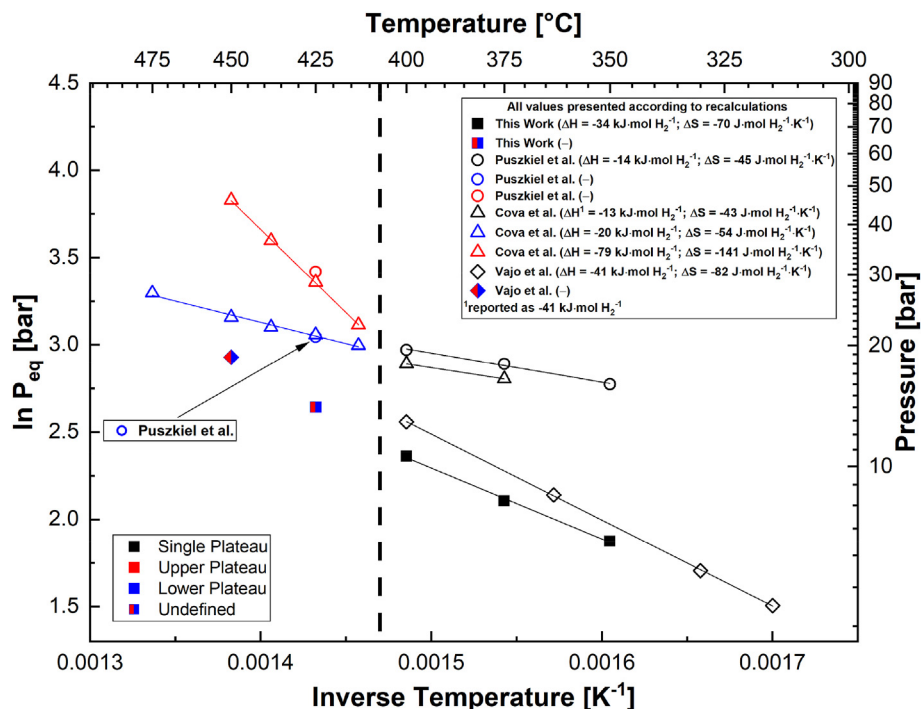
Fig. 2 – Comparative analysis for recalculated equilibrium plateau pressures for absorption reaction and the values of ΔH and ΔS from the cited works [22,23,33][1]. Dashed line divides roughly the one-plateau from the two-plateau expected region.

in our material, but it may be possible that this transition occurs at higher temperatures.

As seen in Fig. 3a), for the hydrogenation process, the obtained values for ΔH and ΔS in this work are -34 ± 2 kJ·mol H_2^{-1} and -70 ± 3 J·K^{-1}·mol H_2^{-1} respectively. The obtained fitting goodness (R^2) of 0.994 shows a proper correlation. It is important to notice that the red-marked point at 425 °C is not considered for the linear fitting. These values are in good agreement with the results published by Vajo et al. [22] for the temperature ranges below 400 °C. In Fig. 1, for the curve at 425 °C, the "bump" seen around 0.55 and the steep increase in the pressure with increased reacted fraction suggests the presence of a second plateau. However, the difference observed here is not comparable to the change that has been reported in the work of Puszkiel [33] and Cova et al. [23]. Additionally, it should be noted that the point at 425 °C (Fig. 3a)) presents a positive deviation over the fitted curve, in agreement with the work of Vajo et al., where the positive deviation is seen at 450 °C [22]. This positive deviation can be ascribed to the presence of a two-plateau region. This issue is not still clear and would require further investigations that are beyond the scope of this work.

In the present work, for the sake of preciseness, a conservative assumption is made to guarantee the validity of the kinetic model in a range in which the mutual hydrogenation of MgB_2 and LiH to $LiBH_4$ and MgH_2 occurs. The temperature range of the kinetic data is limited to 412 °C. Above 412 °C it may be possible that the system undergoes a different reaction pathway, and the kinetic analysis would not be representative. Therefore, the 425 °C kinetic results are, from now on, excluded from the kinetic modeling dataset.

With the calculated values of ΔH and ΔS it is possible to draw a pressure vs. temperature diagram (an exponential form of van't Hoff equation) as seen in Fig. 3b). In this diagram, it is possible to see the equilibrium conditions for the Li-RHC system considering only the results found in the present study. Additionally, the points considered for the development of the kinetic model are shown as round markings.

Additionally, the X-markings seen in Fig. 3b) are the experimentally measured mean plateau pressure values. It is possible to see that there are only small deviations between the values obtained from the van't Hoff equation and the experimental results used for the fit.

The general expression for calculating the equilibrium pressure P_{eq} is given in Eq. (7)) (van't Hoff Equation)

$$\ln(P_{eq}) = \left(\frac{-34 \cdot 10^3 \, J \cdot mol \, H_2^{-1}}{R \cdot T_{mean}} \right) - \left(\frac{-70 \, J \cdot mol \, H_2^{-1} \cdot K^{-1}}{R} \right)$$

(7)

where R is the ideal gas constant, and T_{mean} is the mean temperature throughout the experiment.

---

[1] The reported value of the ΔH in their work of Cova et al. was of -41 ± 4 kJ·mol H_2^{-1} for the single-plateau region. However, by taking the plateau points as described in their work, we were unable to reproduce the results. The points in the graph are being taken from the PCI readings, but as stated, both the recalculated and reported results are being shown here.
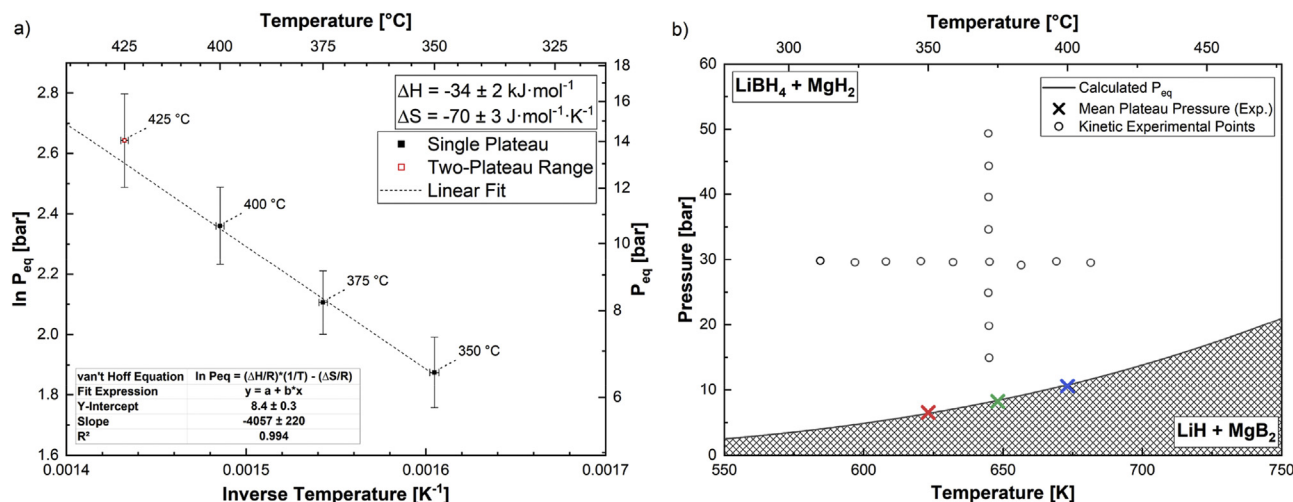
Fig. 3 – a) van't Hoff plot for the PCI data, along with the fitted linear curve and its parameters. Note that the pressure at 425 °C was not used for the fitting. b) equilibrium absorption conditions in P vs T diagram, along with the measured kinetic experimental conditions. The x-markings represent the mean plateau pressure obtained experimentally in Fig. 1.

Modeling of the kinetic behavior

Determination of G(α): gas-solid model

Different reaction models have been developed to represent hydrogenation and dehydrogenation reactions. The models here considered for this purpose can be seen in Table S1 of the Supplementary Material. To deduce which of the reaction models best describes our system under the studied experimental conditions, the general approach is to start evaluating which of the integral equations g(α) (see Table 1) best correlates with the obtained experimental data. In order to do so, the so-called "Sharp and Jones" method (named after the original works of Sharp et al. [49] and Jones et al. [50] and also known as "Reduced Time Method") has been shown to be the most efficient tool, as it gives more parameters for evaluation that help determining how good is the agreement of the experimental data to each of the reaction models. A general description of the employed method has been given in the work of Puszkiel [40].

The evaluation of the best-fitting model is based on the values of three parameters; the coefficient of determination R^2 closest to 1, a Y-axis intercept closest to 0 and a slope closest to 1 [40,49,50]. All results are summarized in Table 2. Further information on how the method was implemented can be seen in the Supplementary Material, along with the figures for all the fittings done in this work (Fig. S3).

All the fittings were performed for the measured temperatures within the range of 312 °C–412 °C under 30 bar of initial H_2-pressure for each of the models. A graphical summary of the results in regards to the models in each temperature can be seen in Fig. S4 of the Supplementary Material.

The obtained results indicate that there are 5 different models that rank sufficiently well in regard to R^2 values, namely, JMAEK with n = 1, JMAEK with n = 1.5, CV, 2-D diffusion limited and 3-D diffusion limited models. However, as slope and Y-intercept agreement are taken into account, both diffusion-limited models cannot be considered as suitable candidates. Regarding the three remaining models,

JMAEK with n = 1.5 has insufficient proximity of the target values for slope and Y-intercept. Slightly closer to the targets is the CV model. Still, the JMAEK with n = 1 has, comparatively, the best match for the two parameters, especially considering Y-intercept.

Taking into account that the JMAEK with n = 1 model presents the highest R^2 values for all the temperatures (range from 0.996 to 0.999) and ranks rather well in the two other parameters, it is from now on assumed to be the most suitable model to describe the kinetics of the system.

For pristine Li-RHC, different authors reported differing models and even rate-limiting steps. In one of the first works related to the determination of rate-limiting steps and reaction models, Wan et al. claimed that the rate-limiting step should be the diffusion of species through the product layer [51]. Differently, Bösenberg et al. argued that an interface-limited model would be a better representation of the system [27]. Later on, Puszkiel et al., in two different studies, argued in favor of an interface-controlled rate-limiting step [34,48]. Le et al. also reported an interface-controlled reaction [25]. Two models with interface-controlled kinetics were presented in these studies; the three-dimensional contracting-volume interface-controlled (3D CV) [27,34] and one-dimensional growth with interface-controlled reaction (JMAEK with n = 1) [25,48]. Although different models have been proposed, it should be noted that these models imply the same rate-limiting step. Furthermore, comparing these previous studies, some remarks should be taken into consideration. First, in some earlier works the JMAEK with n = 1 was not taken into account. Second, the method for determining and evaluating the fitting goodness of the kinetic models became more robust with time, since it became increasingly common practice to employ the Sharp and Jones method [40,48–50].

Concerning the Li-RHC with additives, different models were proposed for the system. Puszkiel et al. reported that, with the addition of 1% mol of TiO_2, the model that best represents the system is the interface-controlled one-dimensional growth (JMAEK with n = 1) [48]. Le et al. reported that for

the Li-RHC with the addition of 0.00625 mol of (3TiCl$_3$·AlCl$_3$), the best-describing model changes in relation to the pristine material and becomes the 3D contracting-volume interface-controlled [25].

Particularly for TiCl$_3$, Bösenberg et al. claimed that by mixing this additive (the amount is not stated), for the second absorption at 350 °C and 50 bar, two possible models could be considered as suitable: the three-dimensional diffusion-controlled contracting-volume (3D CV diffusion-controlled) and the interface-controlled three-dimensional contracting-volume (3D CV interface-controlled) [27]. In their work, though, the JMAEK with n = 1 was not considered as a candidate. Additionally, the so-called reduced-time method based on the works of Sharp et al. [49] and Jones et al. [50] was not employed at the time.

In more recent studies for the 0.05 mol TiCl$_3$-added Li-RHC system it was found that the JMAEK with n = 1 best represents the experimental data [9]. This determination of g(α) was made based on different temperatures between 325 °C and 425 °C under 30 bar of initial H$_2$-pressure [9].

In the present work, by measuring the absorption kinetics in smaller steps (total of 10 measured curves between 312 °C and 425 °C) and by using the results after the 18th absorption cycle, it is reasonable to assume that both the influences of the calculation errors and of the change in hydrogen capacity with the first (de)hydrogenation cycles (altering the time to reach 90% of the reacted fraction) have been accounted for or reduced, respectively.

Considering that the JMAEK with n = 1 model describes a one-dimensional interface-controlled reaction, the results reported on [25,27,34,48] are in line with what is being proposed in this work.

The experimental results for reacted fraction α against time are shown in Fig. 4a) and Fig. 4b). The solid lines represent experimental kinetic data at different temperatures under 30 bar of initial H$_2$-pressure and for different pressures at 375 °C, respectively. The non-linear fit was performed to determine the k-values for the integrated JMAEK expression with n = 1 [44–46], as shown in Eq. (8):

$$\alpha = 1 - \exp(-k \cdot t) \tag{8}$$

The non-linear fitted curves are presented in Fig. 4a) and b) as dashed lines. Both graphs indicate clearly that higher pressures and higher temperatures — as usually expected — result in faster kinetics.

For the curves under a pressure of 30 bar, the non-linear fit performed represents well the experimental results obtained for most temperatures, with only minor observed deviations for the lowest temperatures. This deviation stems from the fact that the expression used for the fitting does not produce curves with inflections, which is observed clearly in the experimental curves for 325 °C and 337 °C in Fig. 4a). Such an aspect has been previously identified also in other works performed on this material [9]. The fitting parameters can be seen in Tables S3 and S4 of the Supplementary Material.

A different kind of misfit between experimental data and fitted results is seen for the kinetic curves at 375 °C. For 15 and 20 bar pressures, the non-linear fits seemingly underestimate the hydrogen uptake during the first minutes of reaction. However, the increase in the reacted fraction for the experimental curves is likely related to an experimental artifact due to the time necessary to close the valve that initially sets the pressure difference between reference and sample holder volumes to zero. For a more in-depth description of the internal workings of the measurement apparatus, see Ref. [38]. It should be considered that the outline of the fitted curve presents a more realistic representation of the kinetics of the material under these experimental conditions than the experimental curve itself. Considering all the described effects, the deviations between the model and the experimental results are negligible. Therefore, it is possible to conclude that the proposed gas-solid model (Eq. (8)) is in good agreement with the experimental results.
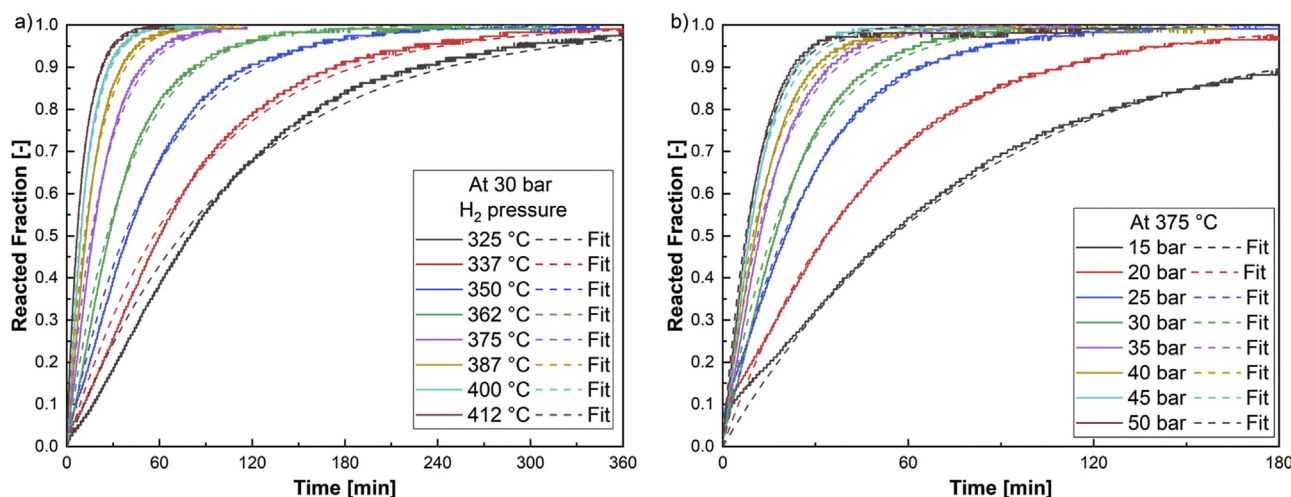

Fig. 4 — Experimental (solid lines) and fitted (dashed lines) curves for reacted fraction against time for a Li-RHC at a) different temperatures under 30 bar of initial H$_2$-pressure, b) at 375 °C under different pressures. Note that time scales are different for each of the plots.

Determination of temperature K(T) and pressure F(P) functionalities

With the values from the k (T, P)-semi-empirical kinetic constants obtained from the non-linear fits of the experimental results from different temperatures under 30 bar initial H_2-pressure, the ln k against the inverse mean temperature are plotted in Fig. 5.

A linear fitting leads to the determination of the apparent activation energy E_a and the frequency factor A. The linear fit presented a proper fitting goodness R^2 of 0.998. The values here found for the frequency factor A and the apparent activation energy E_a were respectively 100 ± 2 kJ·mol H_2^{-1} and $(8.1 \pm 2.6) \cdot 10^4$ s^{-1}.

In order to take into consideration the influence of the experiment pressure P and the mean equilibrium pressure P_{eq} at each temperature, the two found parameters, i.e., E_a and A, are still to be corrected by the driving force component, F(P).

For the evaluation of the different models for F(P), Eq. (5) is divided into both sides by F(P) and combined with Eq. (4) resulting in

$$\frac{k(T, P)}{F(P)} = A \cdot \exp\left(\frac{-E_a}{R \cdot T}\right) \tag{9}$$

Now, by applying natural logarithms to both sides in Eq. (9) and rearranging, it becomes

$$\ln\left[\frac{k(T, P)}{F(P)}\right] = [\ln A] + \left[\frac{-E_a}{R}\right] \cdot \left[\frac{1}{T}\right] \tag{10}$$

with this linearized equation, it is possible to determine a frequency factor A and an apparent activation energy E_a that take the pressure dependency into account by utilizing the values for k (T, P) (previously obtained from the fits shown in Fig. 4), and each of the F(P) expressions. For the F(P) term,

different functionalities are assumed, deducted either from investigations about the thermodynamic behavior or different tentatively proposed ratios and relations between P and P_{eq}. The expressions used in the present work are presented in Table 3.

To take the F(P) component into account, each expression is considered individually and a new plot, analogous to Fig. 5, is built, along with each linear fit. This yields new values for E_a and A for each of the F(P) functionalities, along with the R^2 values for each fitted curve.

Each new set of values for E_a and A are individually considered (see also Supplementary Material Fig. S5). By using the k-values obtained from the fittings shown in Fig. 4 (see also Fig. S6 and Fig. S7 in the Supplementary Material), it is now possible to evaluate the different driving force expressions. Reorganizing (9), the expression

$$\left[\frac{k(T, P)}{A \cdot \exp\left(\frac{-E_a}{R \cdot T}\right)}\right] = F(P) \tag{11}$$

can be obtained, for which the aforementioned values are applied.

Here, each F(P) expression (along with its results A and E_a) can be checked for its validity by plotting and interpreting it graphically. By analogy with a linear equation, the equation's left-hand side is taken as a dependent variable and F(P) as an independent variable. It follows that the best correlation would necessarily have a Y-intercept as near as possible to 0, a slope nearest to 1 and a determination coefficient R^2 closest to 1. For this particular fitting procedure, the linear coefficient is set to 0.

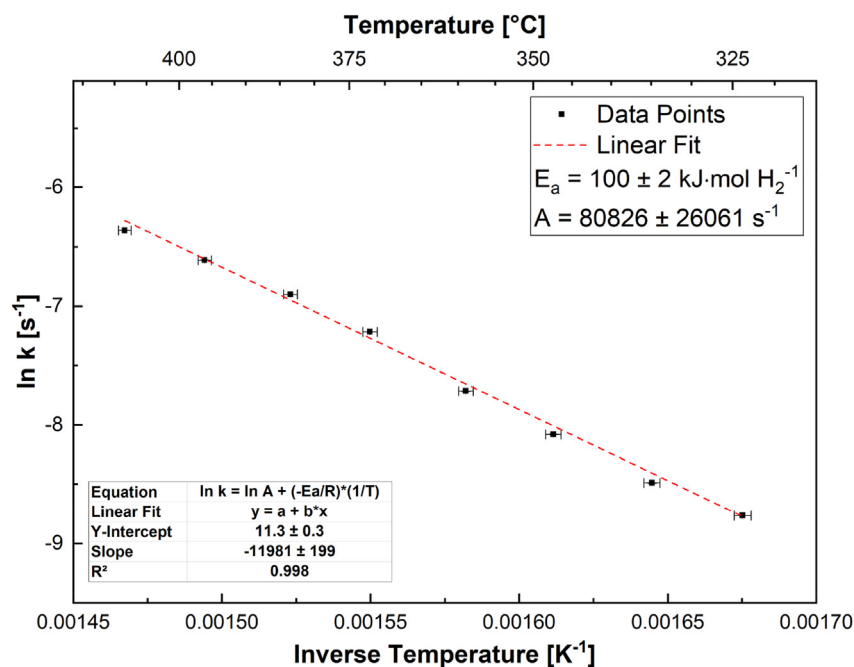The results of this procedure for each F(P) expression can be seen in the Supplementary Material in Fig. S6. The

Fig. 5 – ln k against inverse mean temperature plot for different temperatures. The linear fit of the experimental data points is indicated as a dashed line. The absolute error bars for the Y-axis are not visible due to their small size.

summarized results of these fitting parameters can be seen also in the Supplementary Material, in Fig. S7. Comparatively, two F(P) expressions rank for R^2 much higher than the others, namely, F2 and F3, with R^2 values of around 0.990. These two best-ranking F(P) expressions are shown in Fig. 6a) and b).

The slope for F2 and F3 is respectively 1.05 ± 0.03 and 1.04 ± 0.03. These values are considered sufficiently close to 1, not only because of the method's uncertainty, but also for the comparative evaluation of the results.

However, just by comparing the parameters of the fitting, it is not possible to distinguish which one of the two expressions is the best choice for F(P).

By visual evaluation, it is possible to see that for F3 the deviations of the linear fit are more likely to be spread symmetrically around the fit curve. For F2, most of the deviations are for the high-pressure points and they all have a positive deviation.

As this deviation is more systematic in F2 than in F3, F3 is being favored, as it is less likely to present substantial deviations when calculated for their α values. Another aspect to take into account are the physical phenomena that were considered to propose said driving force expressions.

However, only limited information is currently available in the literature of why these expressions can fit the data of different pressures, as shown in our results. The driving force term of a chemical reaction is usually based on the thermodynamic activity. Considering the hydrogen gas as ideal, for a gas-solid reaction in a metal hydride, the thermodynamic activity is defined as the applied hydrogen partial pressure P divided by the standard pressure P_0 [69]. However, already for simple gas-solid hydride forming reactions, a wide variety of pressure dependence relations are used [58,59,68]. This fact is related to the different hydride forming materials, experimental conditions and rate-limiting steps associated to the F(P) [40]. In the case of complex hydrides, it is well accepted that in general the relation between the applied pressure P and the equilibrium pressure P_{eq} can describe the driving force term for the formation of a

metal hydride. For instance, in the case of $NaAlH_4$, the functionality of the pressure was empirically determined, and the best function was determined as the first order Taylor series' approximation (centered around P_{eq}) of the change of the free energy for the hydrogenation process, i.e., $(P - P_{eq})/P_{eq}$ [57]. Therefore, in the herein investigated and rather complex 2 $LiBH_4$ + MgH_2 hydride system, the nature of the hydride forming materials, experimental conditions (set up) and the determined interface-rate limiting step leads to the F(P)= $(P - P_{eq})/P_{eq}$ as a best-fitting expression based on the above mentioned Taylor series' approximation. Due to its complexity, futher analysis regarding the physical meaning of the driving force term is beyond this work's scope.

The choice of this F(P) expression changes the previously-assumed apparent activation energy E_a from 100 ± 2 to 146 ± 2 $kJ \cdot mol\ H_2^{-1}$ and the frequency factor A from $(8.1 ± 2.6) \cdot 10^4$ to $(1.8 ± 1.0) \cdot 10^8\ s^{-1}$.

General expression and data validation

Considering the calculated apparent activation energy E_a, the frequency factor A, the driving force expression F3, i.e., F(P) = $(P - P_{eq})/P_{eq}$, and the reaction model as JMAEK with n = 1, it is possible to propose a general expression for the studied system within the stated limits of temperature and pressure, i.e. from 325 °C to 412 °C and from 15 bar to 50 bar. Starting from Eq. (3), substituting its components with K(T) as presented in Eq. (5), introducing the suitable expression for JMAEK with n = 1 (as seen in Table 1) and assuming F3 as the driving force expression, Eq. (12) is obtained, which is the differential form of the general kinetics expression.

$$\frac{d\alpha}{dt} = \left[\left(A \cdot \exp\left(\frac{-E_a}{R \cdot T}\right) \right) \cdot \left(\frac{P - P_{eq}}{P_{eq}} \right) \cdot (1 - \alpha) \right] \tag{12}$$

Furthermore, by performing the integration of this expression, it is possible to obtain the integrated form of the equation, and by inputting the numeric values for the determined parameters, one can write the final formula of Eq. (13) as
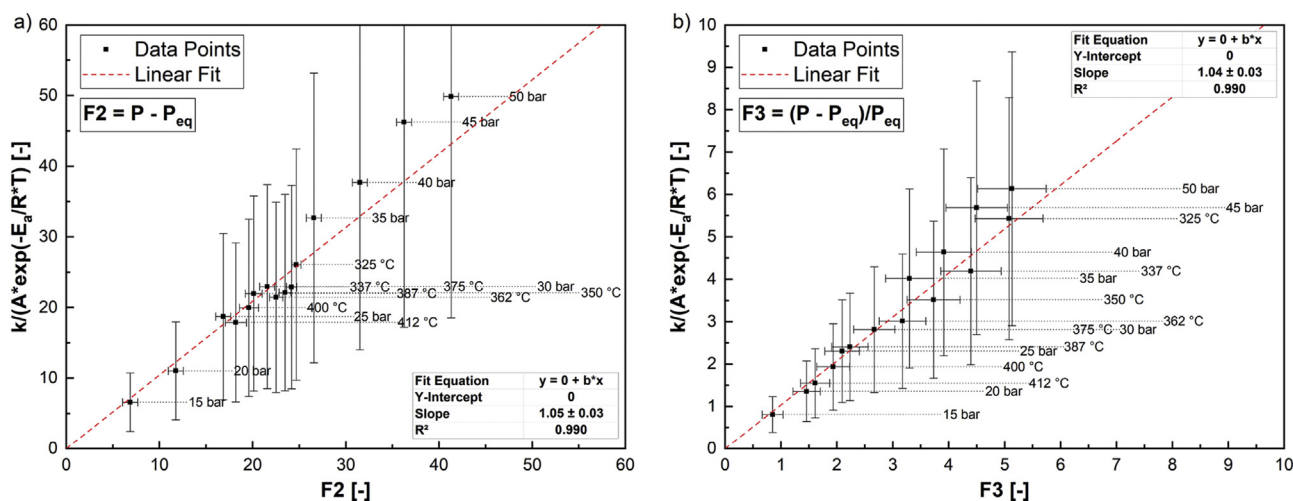

Fig. 6 – Fitting goodness verification for a) F2 and b) F3 driving force expressions.

$$\alpha = 1 - \exp\left[- \left(1.8 \cdot 10^8 \cdot \exp\left(\frac{-146 \cdot 10^3}{8.314 \cdot T} \right) \right) \cdot \left(\frac{P - P_{eq}}{P_{eq}} \right) \cdot t \right]$$

(13)

In this expression, the reacted fraction α varies between 0 and 1, the frequency factor A is given in (s^{-1}), the apparent activation energy E_a is given in $(J \cdot mol\ H_2^{-1})$, the temperature T is given in (K), the pressure P is given in (bar) and the time t is given in (s).

By plotting Eq. (13) with the transformed fraction α against the time t, it is now possible to compare the calculated and the experimental kinetic curves. Fig. 7a) shows the validation plot for the experiments with different temperatures (in the 325–412 °C range) under 30 bar of initial H_2-pressure. In it, the solid lines represent the experimental data and the dashed lines, the calculated values. The insert on the bottom-right corner displays the same data but is limited to the higher temperature curves and the first 60 min of reaction.

For most of the temperature range, a very high degree of correlation between calculated and experimental results is achieved throughout the reaction. However, for the lowest temperatures investigated, e.g., 325 °C and 337 °C, the experimental curves present a perceptible inflection in the first hours, which is related to the significant complexity of the system reaction mechanism. This reaction modeling cannot capture this behavior, as the equations that are used imply a monotonic behavior and a curve that is always concave. Concerning these curves, it is visible that the kinetic reaction rate (curve slope) of the model is higher on the first minutes of reaction, slightly overestimating it when compared to the experimental data. After the inflection point, for most of the temperatures analyzed, the calculated reaction rates now are slightly underestimated. Before reaching the saturation point, the two curves again agree to a significant extent.

The coefficient of determination (R^2) for the calculated model and the experimental results was calculated according to Eq. (S2) of the Supplementary Material (from 0 to 0.99 reacted fraction). The values give a more objective frame of comparison between the curves' goodness-of-fit and possibly serve as a benchmark for other works for the future irrespective of the material used or reaction model proposed. Particularly for the absorption reactions at 375 °C all the R^2 values were above 0.996.

Although small visible differences between the model (Eq. (13)) and the experimental results can be seen, it should still be considered that the applied model has been successful in describing the kinetics of the system, as these deviations can be considered minor in the frame of the course of the reaction. In Fig. 7, it is possible to observe that the model shows a quite good agreement between the calculated and the experimental results with fitting goodness ranging between 0.97 and 0.99.

Thermodynamic stability and kinetic behavior: isokinetic contour graphs

An additional interpretation ofthe thermodynamic and kinetic results presented here is to draw isokinetic contour lines in a pressure-temperature diagram, as shown in Fig. 8. The drawing of the isokinetic contour lines helps to understand how system conditions change influences the kinetic constant. For this purpose, a convenient approach is to represent the expression of the contour lines for different values of P as a function of T with chosen values of the kinetic constant k.

By rearranging Eq. (4), combining it with Eq. (5) as a function of temperature, making pressure the dependent variable, and implementing the F3 expression, it is possible to obtain the expression shown in Eq. (14). For plotting the isokinetic lines, k-values are arbitrarily chosen. Here, A is the frequency factor $(1.8 \cdot 10^8\ s^{-1})$, the apparent activation energy E_a $(146\ kJ \cdot mol\ H_2^{-1})$ and R is the ideal gas constant. The equilibrium pressure P_{eq} is calculated by Eq. (7).
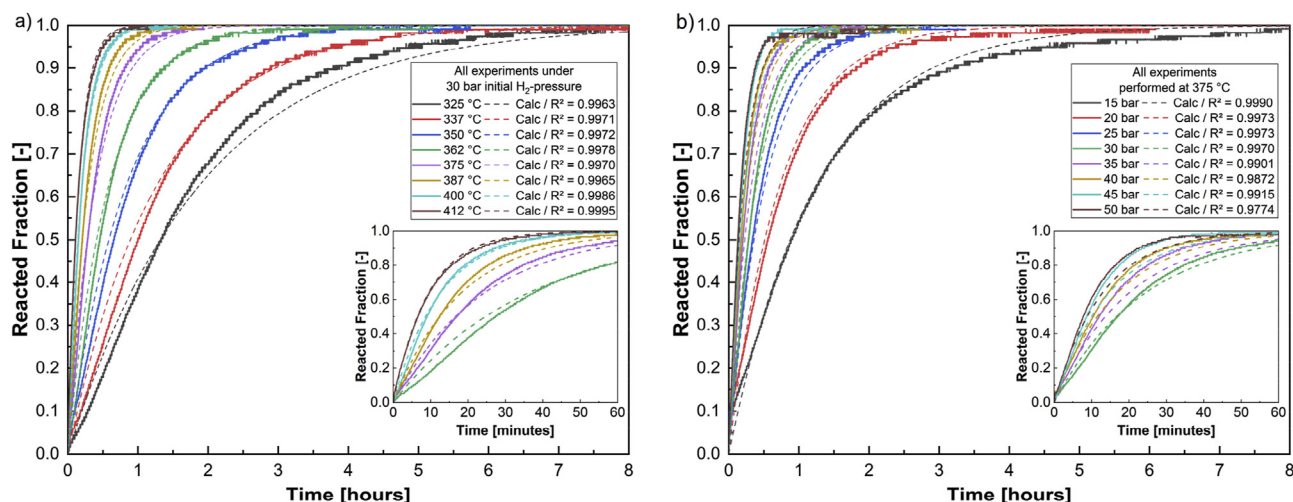

Fig. 7 — Comparison between calculated and experimental data for the variation of reacted fraction along the time for a) different temperatures at 30 bar initial H_2-pressure and b) different pressures at 375 °C along with the calculated coefficient of determination (R^2). The inset diagrams in the figures represent the same data under a shorter time scale.
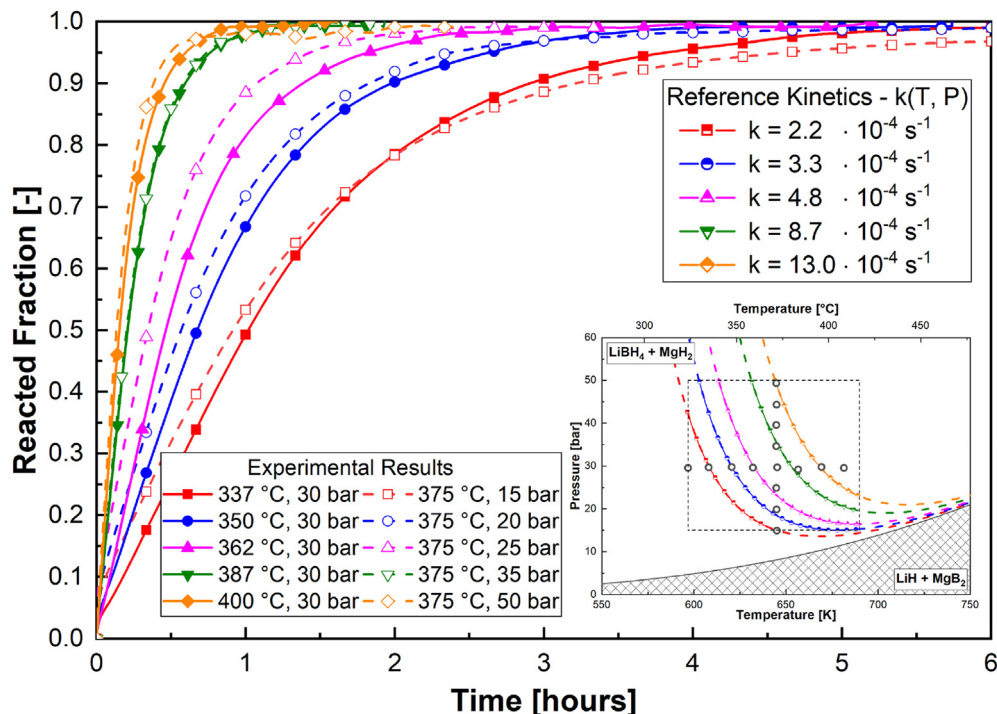
Fig. 8 — Kinetic model validation plot. In the inset diagram, the round circles represent each kinetic measurement at different pressures and temperatures. The delimited area marks the region of validity of the kinetic model. The isokinetic curves that nearly intercept two experimental points are presented. In the main diagram, with the same colors, the experimental data for reacted fraction against time are presented.

$$P = P_{eq} \cdot \left(1 + \left[\frac{k_{cte}}{A \cdot \exp\left(-\frac{E_a}{R \cdot T} \right)} \right] \right) \qquad (14)$$

This expression yields the contour lines seen in the inset graph of Fig. 8 and in Fig. S8 of the Supplementary Material. In both, the hatched region (below equilibrium curve) represents the equilibrium conditions that favor the stability of LiH + MgB$_2$, and the region above, in which the stable phases are LiBH$_4$ and MgH$_2$. This equilibrium line has been calculated using the van't Hoff equation (Eq. (7)) with the values of ΔH and ΔS obtained in the present work.

The curves drawn in the absorbed state region (LiBH$_4$ and MgH$_2$) are the isokinetic lines obtained from Equation (14). The values in Fig. 8 were chosen to identify the experimental conditions in which at least two points are nearly intercepted by a single isokinetic line. In Fig. S8, the values were chosen in order to show how the kinetic constant k (T, P) varies as a function of T and P.

The region in which the model is expected to reliably describe the kinetic behavior of the Li-RHC under absorption conditions is schematically shown in Fig. 8 as a square limited by the temperature and pressure conditions for which this model is deemed valid. Thus, inside this region, the calculated isokinetic contour lines are solid, and outside the region, they are dashed lines, indicating that, in principle, the shape of these curves can be known with reasonable precision only inside this validity region.

The lower temperature border is around 325 °C, since, as shown in Table 2 (and in Fig. S3 and Fig. S4 of the Supplementary Material), the JMAEK with n = 1 does not fit well the kinetic curve at 312 °C. On the higher-temperature side (above 412 °C), the temperature range is limited by the change of the reaction pathway, resulting in different equilibrium conditions. In relation to the pressure limits, it is possible to assume that in the lower pressure range, if enough separation between the system conditions and the equilibrium condition (P$_{eq}$ curve) occurs, the model can still represent the kinetics of the system consistently. However, no experimental validation has been performed below 15 bar, not only because the times for the kinetics would be significantly large, but also because one of the goals of this work is to describe with enough detail the region (for conditions of P and T) that is of interest for potential applications of this material in energy storage systems. In the high-pressure region (above 50 bar), it is expected that the results obtained from the model can still represent the experimental results to some extent. However, as kinetics get faster in experimental conditions with a more significant driving force, it becomes increasingly harder to evaluate experimental results, as relatively small experimental uncertainties and experimental artifacts of measurement (valves opening/closing times and pressure transducer stabilization, *inter alia*) can lead to a significant change in the outcome and alter the interpretation of the results.

For each of the isokinetic curves drawn in the inset graph in Fig. 8, the nearly intercepted experimental curves under these conditions are shown in the main graph. As these

matching curves show very similar curve outlines, it has been shown that the found isokinetic line expression is able to reproduce the kinetic behavior of the material inside the aforementioned validity region quite well.

Still, it should be taken into consideration that the pressure and temperature ranges that delimit the validity of the model in this work are conservatively taken. That is, while the physical explanations provided to the kinetic model should hold true only in these ranges, extrapolation of the model to close-enough neighboring regions still yield excellent prediction capabilities (not shown here), showing the mathematical robustness of the model even for extended temperature and pressure conditions.

Conclusion and outlook

In this work, both thermodynamic and kinetic experimental data are analyzed in detail for the $LiBH_4/MgH_2$ Reactive Hydride Composite (Li-RHC) with 0.05 $TiCl_3$ additive under absorption conditions. The obtained results in the range between 350 °C and 400 °C for ΔH and ΔS are -34 ± 2 kJ·mol H_2^{-1} and of -70 ± 3 J·K^{-1}·mol H_2^{-1}, respectively, in good agreement with previously reported values.

To the best of our knowledge, it is the first time that a comprehensive kinetic model under absorption conditions is developed for the Li-RHC by using the separable variable method. Applying this model, the effects of temperature, pressure and transformation of the hydride forming material are considered in the rate expression. The results indicate that the transformation of the forming hydride is limited by the movement of the not-hydrogenated/hydrogenated material interface, described by the one-dimensional interface-controlled model with a fixed number of nuclei and constant interface velocity, also known as JMAEK with n = 1 model. After taking the driving force component into account, the apparent activation energy E_a and pre-exponential factor A are, respectively, $(1.8 \pm 1.0)\cdot 10^8$ s^{-1} and 146 ± 3 kJ·mol H_2^{-1}.

The developed model successfully describes the intrinsic kinetic behavior of the system, with only minor observed deviations. For the considered range of temperatures and pressures, the model shows fitting goodness ranging from 0.97 to 0.99. On-going research is being done to comprehensively describe the desorption kinetic behavior of the here studied material. Moreover, the developed models will be applied to model pilot-plant sized energy-hydrogen storage tanks through FEM simulations to better understand and optimize their designs.

The model presented here indicates that absorption times for the studied material are in the range of hours. While faster kinetics is a desirable trait for hydrogen storage materials, its influence on the performance of hydrogen storage systems depends heavily on the size and on the design choices for such systems [39]. For instance, intrinsic kinetics becomes increasingly unimportant as the size of the system increases. Still, the kinetic behavior is a core element of the functionally of these systems and needs to be properly described in order to obtain accurate descriptions of the combined effects that occur in these bigger-scale systems. However, faster kinetics

have been demonstrated for Li-RHC in previous works. It has been previously demonstrated, that by producing ball-milled powders with some additives, it was possible to obtain nanostructures with in-situ-formed catalysts such as Li_xTiO_2 and AlTi compounds that enable the completion of the hydrogenation reaction with times of less than 30 min under 400 °C and 50 bar [25,48]. Our expectations are, that since in these cases the rate-limiting step has been also identified as interface-controlled, the modelling approach here presented can be similarly applied to describe these materials with improved kinetic behavior.

Declaration of competing interest

The authors declare that they have no known competing financial interests or personal relationships that could have appeared to influence the work reported in this paper.

Acknowledgements

Appendix A. Supplementary data

Supplementary data to this article can be found online at https://doi.org/10.1016/j.ijhydene.2021.06.227.

REFERENCES

[1] The national hydrogen strategy. 2020. Accessed: Dez. 11, 2020. Available online: https://www.bmwi.de/Redaktion/EN/Publikationen/Energie/the-national-hydrogen-strategy.html.

[2] Weger L, Abánades A, Butler T. Methane cracking as a bridge technology to the hydrogen economy. Int J Hydrogen Energy 2017;42:720–31. https://doi.org/10.1016/j.ijhydene.2016.11.029.

[3] Dincer I, Acar C. Review and evaluation of hydrogen production methods for better sustainability. Int J Hydrogen Energy 2015;40:11094–111. https://doi.org/10.1016/j.ijhydene.2014.12.035.

[4] Weaver G. World fuel cells - an industry profile with market prospects to 2010. 1st ed. Elsevier Science; 2002.

[5] Dalebrook AF, Gan W, Grasemann M, Moret S, Laurenczy G. Hydrogen storage: beyond conventional methods. Chem Commun 2013;49:8735. https://doi.org/10.1039/c3cc43836h.

[6] Department of Energy of the United States of America. Energy requirements for hydrogen gas compression and liquefaction as related to vehycle storage needs. 2009.

[7] Züttel A. Materials for hydrogen storage. Mater Today 2003;6:23–33. https://doi.org/10.1016/S1369-7021(03)00922-2.

[8] Lemmon EW, McLinden MO, Friend DG Thermophysical Properties of Fluid Systems. In: Linstrom P.J., editor. NIST Chemistry WebBook, NIST Standard Reference Database Number 69. Gaithersburg MD, 20899: National Institute of Standards and Technology. doi:10.18434/T4D303

[9] Jepsen J, Milanese C, Puszkiel J, Girella A, Schiavo B, Lozano G, et al. Fundamental material properties of the 2LiBH$_4$-MgH$_2$ reactive hydride composite for hydrogen storage: (II) kinetic properties. Energies 2018;11:1170. https://doi.org/10.3390/en11051170.

[10] Pacific Northwest National Laboratory. Lower and higher heating values of hydrogen and other fuels. Available online: https://h2tools.org/hyarc/hydrogen-data/lower-and-higher-heating-values-hydrogen-and-other-fuels; 2020.

[11] Puszkiel JA, Andrade-Gamboa JJ, Gennari FC. Recent progress in Mg–Co–H and Mg–Fe–H systems for hydrogen energy storage applications. In: Emerging materials for energy conversion and storage. Elsevier; 2018. p. 393–428. https://doi.org/10.1016/B978-0-12-813794-9.00012-0.

[12] Ren J, Musyoka NM, Langmi HW, Mathe M, Liao S. Current research trends and perspectives on materials-based hydrogen storage solutions: a critical review. Int J Hydrogen Energy 2017;42:289–311. https://doi.org/10.1016/j.ijhydene.2016.11.195.

[13] Schlesinger HI, Brown HC. Metallo borohydrides. III. Lithium borohydride. J Am Chem Soc 1940;62:3429–35. https://doi.org/10.1021/ja01869a039.

[14] Schlapbach L, Züttel A. Hydrogen-storage materials for mobile applications. Nature 2001;414:353–8. https://doi.org/10.1038/35104634.

[15] Züttel A, Wenger P, Rentsch S, Sudan P, Mauron Ph, Emmenegger Ch. LiBH$_4$ a new hydrogen storage material. J Power Sources 2003;118:1–7. https://doi.org/10.1016/S0378-7753(03)00054-5.

[16] Orimo S, Nakamori Y, Kitahara G, Miwa K, Ohba N, Towata S, et al. Dehydriding and rehydriding reactions of LiBH$_4$. J Alloys Compd 2005;404–406:427–30. https://doi.org/10.1016/j.jallcom.2004.10.091.

[17] Barkhordarian G, Klassen T, Dornheim M, Bormann R. Unexpected kinetic effect of MgB$_2$ in reactive hydride composites containing complex borohydrides. J Alloys Compd 2007;440:L18–21. https://doi.org/10.1016/j.jallcom.2006.09.048.

[18] Puszkiel J, Gasnier A, Amica G, Gennari F. Tuning LiBH4 for hydrogen storage: destabilization, additive, and nanoconfinement approaches. Molecules 2019;25:163. https://doi.org/10.3390/molecules25010163.

[19] Lin W, Xiao X, Wang X, Wong J-W, Yao Z, Chen M, et al. Extreme high reversible capacity with over 8.0 wt% and excellent hydrogen storage properties of MgH$_2$ combined with LiBH$_4$ and Li$_3$AlH$_6$. J Energy Chem 2020;50:296–306. https://doi.org/10.1016/j.jechem.2020.03.076.

[20] Ding Z, Li H, Shaw L. New insights into the solid-state hydrogen storage of nanostructured LiBH$_4$-MgH$_2$ system. Chem Eng J 2020;385:123856. https://doi.org/10.1016/j.cej.2019.123856.

[21] Dansirima P, Thiangviriya S, Plerdsranoy P, Utke O, Utke R. Small hydrogen storage tank filled with 2LiBH$_4$ MgH$_2$ nanoconfined in activated carbon: reaction mechanisms and performances. Int J Hydrogen Energy 2019;44:10752–62. https://doi.org/10.1016/j.ijhydene.2019.02.178.

[22] Vajo JJ, Skeith SL, Mertens F. Reversible storage of hydrogen in destabilized LiBH$_4$. J Phys Chem B 2005;109:3719–22. https://doi.org/10.1021/jp040769o.

[23] Cova F, Rönnebro ECE, Choi YJ, Gennari FC, Larochette PA. New insights into the thermodynamic behavior of 2LiBH$_4$ –MgH$_2$ composite for hydrogen storage. J Phys Chem C 2015;119:15816–22. https://doi.org/10.1021/acs.jpcc.5b02047.

[24] Jepsen J, Milanese C, Puszkiel J, Girella A, Schiavo B, Lozano G, et al. Fundamental material properties of the 2LiBH$_4$-MgH$_2$ reactive hydride composite for hydrogen storage: (I) thermodynamic and heat transfer properties. Energies 2018;11:1081. https://doi.org/10.3390/en11051081.

[25] Le T-T, Pistidda C, Puszkiel J, Castro Riglos MV, Karimi F, Skibsted J, et al. Design of a nanometric AlTi additive for MgB$_2$-based reactive hydride composites with superior kinetic properties. J Phys Chem C 2018;122:7642–55. https://doi.org/10.1021/acs.jpcc.8b01850.

[26] Puszkiel J, Gennari FC, Arneodo Larochette P, Troiani HE, Karimi F, Pistidda C, et al. Hydrogen storage in Mg–LiBH$_4$ composites catalyzed by FeF$_3$. J Power Sources 2014;267:799–811. https://doi.org/10.1016/j.jpowsour.2014.05.130.

[27] Bösenberg U, Kim JW, Gosslar D, Eigen N, Jensen TR, Bellosta von Colbe JM, et al. Role of additives in LiBH$_4$–MgH$_2$ reactive hydride composites for sorption kinetics. Acta Mater 2010;58:3381–9. https://doi.org/10.1016/j.actamat.2010.02.012.

[28] Bösenberg U, Doppiu S, Mosegaard L, Barkhordarian G, Eigen N, Borgschulte A, et al. Hydrogen sorption properties of MgH$_2$–LiBH$_4$ composites. Acta Mater 2007;55:3951–8. https://doi.org/10.1016/j.actamat.2007.03.010.

[29] Karimi F, Riglos MVC, Santoru A, Hoell A, Raghuwanshi VS, Milanese C, et al. In situ formation of TiB$_2$ nanoparticles for enhanced dehydrogenation/hydrogenation reaction kinetics of LiBH$_4$ –MgH$_2$ as a reversible solid-state hydrogen storage composite system. J Phys Chem C 2018;122:11671–81. https://doi.org/10.1021/acs.jpcc.8b02258.

[30] Xiao X, Wang S, Tu G, Zhang L, Fan X, Li S, et al. Enhanced reversible hydrogen storage performance of NbCl$_5$ doped 2LiH–MgB$_2$ composite. Int J Hydrogen Energy 2014;39:2132–41. https://doi.org/10.1016/j.ijhydene.2013.11.091.

[31] Zhang Y, Morin F, Huot J. The effects of Ti-based additives on the kinetics and reactions in LiH/MgB$_2$ hydrogen storage system. Int J Hydrogen Energy 2011;36:5425–30. https://doi.org/10.1016/j.ijhydene.2011.01.135.

[32] Saldan I, Campesi R, Zavorotynska O, Spoto G, Baricco M, Arendarska A, et al. Enhanced hydrogen uptake/release in 2LiH–MgB$_2$ composite with titanium additives. Int J Hydrogen Energy 2012;37:1604–12. https://doi.org/10.1016/j.ijhydene.2011.10.047.

[33] Puszkiel JA. Preparación, estudio y optimización de hidruros complejos para almacenamiento de hidrógeno. Doctoral Thesis. Universidade Nacional de Cuyo; 2012.

[34] Puszkiel JA, Gennari FC, Larochette PA, Ramallo-López JM, Vainio U, Karimi F, et al. Effect of Fe additive on the hydrogenation-dehydrogenation properties of 2LiH + MgB$_2$/2LiBH$_4$ + MgH$_2$ system. J Power Sources 2015;284:606–16. https://doi.org/10.1016/j.jpowsour.2015.02.153.

[35] Jepsen J, Capurso G, Puszkiel J, Busch N, Werner T, Milanese C, et al. Effect of the process parameters on the energy transfer during the synthesis of the 2LiBH$_4$-MgH$_2$ reactive hydride composite for hydrogen storage. Metals 2019;9:349. https://doi.org/10.3390/met9030349.

[36] Jepsen J, Milanese C, Girella A, Lozano GA, Pistidda C, Bellosta von Colbe JM, et al. Compaction pressure influence on material properties and sorption behaviour of LiBH$_4$–MgH$_2$ composite. Int J Hydrogen Energy 2013;38:8357–66. https://doi.org/10.1016/j.ijhydene.2013.04.090.

[37] Wang C-S, Brinkerhoff J. Predicting hydrogen adsorption and desorption rates in cylindrical metal hydride beds: empirical correlations and machine learning. Int J Hydrogen Energy 2021;46:24256–70.

[38] Schulz R, Boily S, Huot J. Appareils pour la titration des gaz et le cyclage d'un matériau absorbant ou adsorbant. 2009. CA 2207149.

[39] Lozano GA, Bellosta von Colbe JM, Klassen T, Dornheim M. Transport phenomena versus intrinsic kinetics: hydrogen sorption limiting sub-process in metal hydride beds. Int J Hydrogen Energy 2014;39. https://doi.org/10.1016/j.ijhydene.2014.09.035. 18952–7.

[40] Puszkiel JA. Tailoring the kinetic behavior of hydride forming materials for hydrogen storage. In: Rahman M, Mohammed Asiri A, editors. Gold nanoparticles - reaching new heights. IntechOpen; 2019. https://doi.org/10.5772/intechopen.82433.

[41] Khawam A, Flanagan DR. Solid-state kinetic models: basics and mathematical fundamentals. J Phys Chem B 2006;110:17315–28. https://doi.org/10.1021/jp062746a.

[42] Stoch L. Structural thermochemistry of solids. Thermochim Acta 1989;148:149–64. https://doi.org/10.1016/0040-6031(89)85211-6.

[43] Martin M, Gommel C, Borkhart C, Fromm E. Absorption and desorption kinetics of hydrogen storage alloys. J Alloys Compd 1996;238:193–201. https://doi.org/10.1016/0925-8388(96)02217-7.

[44] Avrami M. Kinetics of phase change. I general theory. J Chem Phys 1939;7:1103–12. https://doi.org/10.1063/1.1750380.

[45] Avrami M. Kinetics of phase change. II transformation-time relations for random distribution of nuclei. J Chem Phys 1940;8:212–24. https://doi.org/10.1063/1.1750631.

[46] Avrami M. Granulation, phase change, and microstructure kinetics of phase change. III. The Journal of Chemical Physics 1941;9:177–84. https://doi.org/10.1063/1.1750872.

[47] Pang Y, Li Q. A review on kinetic models and corresponding analysis methods for hydrogen storage materials. Int J Hydrogen Energy 2016;41:18072–87. https://doi.org/10.1016/j.ijhydene.2016.08.018.

[48] Puszkiel JA, Castro Riglos MV, Ramallo-López JM, Mizrahi M, Karimi F, Santoru A, et al. A novel catalytic route for hydrogenation–dehydrogenation of 2LiH + MgB$_2$ via in situ formed core–shell Li$_x$TiO$_2$ nanoparticles. J Mater Chem 2017;5:12922–33. https://doi.org/10.1039/C7TA03117C.

[49] Sharp JH, Brindley GW, Achar BNN. Numerical data for some commonly used solid state reaction equations. J Am Ceram Soc 1966;49:379–82. https://doi.org/10.1111/j.1151-2916.1966.tb13289.x.

[50] Jones LF, Dollimore D, Nicklin T. Comparison of experimental kinetic decomposition data with master data using a linear plot method. Thermochim Acta 1975;13:240–5. https://doi.org/10.1016/0040-6031(75)80085-2.

[51] Wan X, Markmaitree T, Osborn W, Shaw LL. Nanoengineering-enabled solid-state hydrogen uptake and release in the LiBH$_4$ + MgH$_2$ system. J Phys Chem C 2008;112:18232–43. https://doi.org/10.1021/jp8033159.

[52] Nam J, Ko J, Ju H. Three-dimensional modeling and simulation of hydrogen absorption in metal hydride hydrogen storage vessels. Appl Energy 2012;89:164–75. https://doi.org/10.1016/j.apenergy.2011.06.015.

[53] Rudman PS. Hydriding and dehydriding of kinetics. J Less Common Met 1983;89:93–110. https://doi.org/10.1016/0022-5088(83)90253-9.

[54] Song MY, Pezat M, Darriet B, Hagenmuller P. A kinetics study of the H-(Mg$_2$Ni-2.7 wt. %Ni) system. J Less Common Met 1984;103:145–52. https://doi.org/10.1016/0022-5088(84)90373-4.

[55] Kim S-R, Lee J-Y. The effect of thermal cycling on the hydriding rate of MmNi$_{4.5}$Al$_{0.5}$. J Less Common Met 1990;161:37–47. https://doi.org/10.1016/0022-5088(90)90312-8.

[56] Goodell PD, Rudman PS. Hydriding and dehydriding rates of the LaNi$_5$-H system. J Less Common Met 1983;89:117–25. https://doi.org/10.1016/0022-5088(83)90255-2.

[57] Lozano GA, Ranong CN, Bellosta von Colbe JM, Bormann R, Fieg G, Hapke J, et al. Empirical kinetic model of sodium alanate reacting system (I). Hydrogen absorption. Int J Hydrogen Energy 2010;35:6763–72. https://doi.org/10.1016/j.ijhydene.2010.04.080.

[58] Lee Jai Young, Byun SM, Park CN, Park JK. A study of the hydriding kinetics of TiFe and its alloys. J Less Common Met 1982;87:149–64. https://doi.org/10.1016/0022-5088(82)90050-9.

[59] Fernández JF, Sánchez CR. Rate determining step in the absorption and desorption of hydrogen by magnesium. J Alloys Compd 2002;340:189–98. https://doi.org/10.1016/S0925-8388(02)00120-2.

[60] Dinachandran L, Mohan G. Numerical simulation of the parametric influence on the wall strain distribution of vertically placed metal hydride based hydrogen storage container. Int J Hydrogen Energy 2015;40:5689–700. https://doi.org/10.1016/j.ijhydene.2015.02.067.

[61] El Mghari H, Huot J, Xiao J. Analysis of hydrogen storage performance of metal hydride reactor with phase change materials. Int J Hydrogen Energy 2019;44:28893–908. https://doi.org/10.1016/j.ijhydene.2019.09.090.

[62] Gwak G, Kim M, Oh K, Kyoung S, Ferekh S, Ju H. Analyzing effects of volumetric expansion of uranium during hydrogen absorption. Int J Hydrogen Energy 2017;42:3723–30. https://doi.org/10.1016/j.ijhydene.2016.08.176.

[63] Mellouli S, Askri F, Dhaou H, Jemni A, Ben Nasrallah S. A study of the thermal behavior of a deformable metal-hydride bed. Int J Hydrogen Energy 2016;41:1711–24. https://doi.org/10.1016/j.ijhydene.2015.10.058.

[64] Uchida HH, Fromm E. H$_2$ absorption rate of titanium films contaminated with increasing amounts of N$_2$, H$_2$0, CO, CO$_2$, CH$_4$ and SO$_2$. Z Phys Chem 1989;164:1123–8. https://doi.org/10.1524/zpch.1989.164.Part_2.1123.

[65] Bernauer O, Töpler J, Noréus D, Hempelmann R, Richter D. Fundamentals and properties of some Ti/Mn based Laves phase hydrides. Int J Hydrogen Energy 1989;14:187–200. https://doi.org/10.1016/0360-3199(89)90053-0.

[66] Rudman PS. Hydrogen-diffusion-rate-limited hydriding and dehydriding kinetics. J Appl Phys 1979;50:7195–9. https://doi.org/10.1063/1.325831.

[67] Karty A, Grunzweig-Genossar J, Rudman PS. Hydriding and dehydriding kinetics of Mg in a Mg/Mg$_2$ Cu eutectic alloy: pressure sweep method. J Appl Phys 1979;50:7200–9. https://doi.org/10.1063/1.325832.

[68] Ron M. The normalized pressure dependence method for the evaluation of kinetic rates of metal hydride formation/decomposition. J Alloys Compd 1999;283:178–91. https://doi.org/10.1016/S0925-8388(98)00859-7.

[69] Hirscher M, editor. Handbook of hydrogen storage: new materials for future energy storage. Weinheim, Germany: Wiley-VCH Verlag GmbH & Co. KGaA; 2010. https://doi.org/10.1002/9783527629800.